Lab on a Chip

PAPER

View Article Online
View Journal

Cite this: DOI: 10.1039/d5lc01117e

Low-temperature inkjet-printed electrochemical sensors on OSTE+ microfluidics for oxygen monitoring and scavenging

Denise Marrero, [ab] Ferran Pujol-Vila,[a] Eva Tuset,[a] Gemma Gabriel, [ab] Rosa Villa,[ab] Mar Alvarez*[ab] and Xavi Illa *[ab]

Real-time monitoring of biological processes is crucial for advancing organ-on-a-chip (OoC) and microphysiological systems (MPS) toward more predictive models for drug development, disease modeling, and precision medicine. Achieving this capability requires robust sensor integration strategies that are compatible with the polymers and substrates used in OoC and MPS platforms. Off-stoichiometry thiol-ene-epoxy (OSTE+) polymers are promising material substrates for sensor integration because of their unreacted thiol groups, which enable strong metal affinity for robust sensor integration and intrinsic oxygen scavenging for microscale oxygen control. However, sensor integration is limited by the high-temperature requirements of conventional metal ink sintering. This work introduces a versatile, low-temperature fabrication strategy that combines inkjet printing with photonic curing to directly sinter gold and silver nanoparticle inks on OSTE+ substrates. This method prevents thermal damage, maintains the chemical functionality and mechanical integrity of the polymer. Electrochemical sensors were integrated into microfluidic devices that enable real-time monitoring of dissolved oxygen, quantitatively capturing the intrinsic oxygen-scavenging behavior of the material. These findings demonstrate a robust route for sensor integration in OSTE+, enhancing real-time monitoring in OoC and MPS platforms.

Received 3rd December 2025,
Accepted 24th March 2026

DOI: 10.1039/d5lc01117e

rsc.li/loc

Introduction

The integration of sensors into microfluidic systems, particularly microphysiological systems (MPSs) and organ-on-a-chip (OoC) platforms, is essential for real-time, on-chip monitoring of dynamic biological events.[1,2] These events are often difficult to assess *via* conventional techniques, including microscopy, biochemical assays, and culture-based methods.[3,4] Such approaches provide valuable end-point or bulk measurements, but they often require off-chip processing that delays decision-making, and some rely on experimental termination, which prevents capturing transient responses and limits spatiotemporal resolution. Despite significant advances in sensor technologies, including electrical,[5–7] electrochemical,[8–10] optical,[11–13] and mechanical sensors,[14,15] their integration into microfluidic platforms remains challenging. Key challenges include poor adhesion of conductive materials to polymeric substrates, incompatibility of fabrication methods with thermally or chemically sensitive materials, and sensor delamination during long-term culture. Existing approaches, such as bonding commercial sensors to chambers or introducing wires through device walls,[16–18] compromise device miniaturization, limit multiplexing, and often introduce leakage or contamination risks. Addressing these limitations is critical to fully realizing the potential of MPS and OoC platforms for applications in drug testing, disease modeling, and precision medicine.

Among the materials commonly used in microfluidic devices, polydimethylsiloxane (PDMS) is still the gold standard polymer for device fabrication due to its biocompatibility, optical transparency, flexibility, and ease of processing *via* soft lithography. Despite its advantages, it presents several drawbacks both for biological modeling and sensor integration. PDMS is prone to absorbing small molecules, such as drugs, which can alter their bioavailability and compromise assay accuracy.[19] Additionally, its low surface energy and chemically inert methyl groups result in poor adhesion to metals, posing challenges for robust and stable sensor integration.[20] To address these limitations, hybrid fabrication strategies often incorporate materials with better adhesion to metals for electrode integration, while maintaining PDMS for other structural components. Metal patterning on PDMS remains challenging due to poor adhesion, often necessitating surface

[a] *Institut de Microelectrònica de Barcelona (IMB-CNM, CSIC), Campus UAB, Bellaterra (Cerdanyola del Vallès), 08193 Barcelona, Spain.*
E-mail: mar.alvarez@imb-cnm.csic.es, xavier.illa@imb-cnm.csic.es
[b] *Centro de Investigación Biomédica en Red en Bioingeniería Biomateriales y Nanomedicina (CIBER-BBN), Madrid 50018, Spain*

modifications such as oxygen plasma or the deposition of adhesion-promoting layers.[21,22] However, these approaches typically provide only temporary adhesion due to surface hydrophobic recovery and mechanical stress-induced delamination.[23] This limitation underscores the need for alternative materials that support both stable sensor integration and compatibility with cell culture environments.

Among these alternatives, off-stoichiometry thiol-ene-epoxy (OSTE+) polymers have emerged as a promising substitute for PDMS.[24,25] OSTE+ polymers are thermosetting materials that can also be fabricated *via* soft lithography. They are synthesized from allyl, thiol, and epoxy monomers in an off-stoichiometric ratio and are cross-linked *via* UV-initiated click chemistry. A key advantage of OSTE+ lies in its two-step fabrication process. After the initial UV-induced polymerization, a partially cured polymer network is formed, leaving reactive groups (thiols or epoxies) available for postprocessing steps such as functionalization and bonding.[26–28] This is followed by a thermal curing step at 110 °C, which completes the crosslinking reaction, resulting in a fully cured material. Unlike PDMS, OSTE+ polymers exhibit minimal absorption of small molecules, which is advantageous for applications involving drug transport studies.[29] Additionally, the strong affinity of thiol groups for noble metals, such as gold and silver, makes OSTE+ polymers a promising substrate for sensor integration, supporting stable monitoring in MPS and OoC systems.[30,31] Moreover, OSTE+ polymers possess intrinsic oxygen scavenging properties, which can be used to regulate oxygen levels in MPS and OoC devices, offering a potential advantage in hypoxia and physiological microenvironment modeling.[32,33] This property originates from the presence of unreacted thiol groups at the surface and within the bulk material.[34] This oxygen scavenging capability was first explored by Sticker and colleagues in 2019 for cell culture applications, where the temperature of the thermal cure was adjusted to tune the oxygen scavenging efficiency.[35] Notably, oxygen scavenging efficiency is inversely correlated with curing temperatures ranging from 110 °C to room temperature, with lower temperatures enhancing this property.

Despite the potential of OSTE+ for sensor integration, developing a room-temperature fabrication strategy to maximize the oxygen scavenging properties of OSTE+ polymers while avoiding harsh chemicals and mechanical stress remains challenging. Rapid prototyping techniques, such as noncontact inkjet printing, offer a viable solution. Inkjet printing enables precise deposition of functional inks without the need for masks, facilitating rapid sensor prototyping under gentle conditions while minimizing material waste. However, a key limitation is its reliance on thermal sintering, which is typically performed at temperatures of approximately 120–150 °C.[10] This restricts the choice of materials to those with a glass transition temperature above the sintering temperature, rendering it incompatible with OSTE+ polymers. To address these limitations, photonic sintering has emerged as a promising alternative. This technique uses high-energy flash lamps to deliver intense, localized light pulses that rapidly sinter thin films without exposing temperature-sensitive substrates to the high temperatures used in conventional thermal processes.[36] By enabling solvent evaporation and metal particle sintering in milliseconds, photonic curing minimizes thermal stress, making it an ideal curing strategy for integrating sensors into temperature-sensitive materials.

This work introduces a low-temperature fabrication strategy that combines inkjet printing with photonic curing to integrate electrochemical sensors onto OSTE+ polymer. Given that OSTE+ has oxygen scavenging capabilities at the microscale, electrochemical sensors were integrated to enable real-time monitoring of dissolved oxygen. Gold and silver nanoparticle inks were deposited *via* inkjet printing and sintered *via* photonic curing, yielding three-electrode electrochemical sensors directly on OSTE+. To validate the sintering approach, electrodes fabricated on polyethylene terephthalate (PET) were used to compare the electrical performance of photonic *versus* conventional thermal sintering. The optimized process was then applied to the OSTE+ substrate to fabricate oxygen sensors that were integrated into a microfluidic device. Real-time dissolved oxygen levels were monitored for 18 h at three distinct locations within the microchannel, demonstrating the spatial resolution and temporal stability of the sensors. By avoiding bulk thermal exposure during sintering, this low-temperature fabrication strategy expands the potential for sensor integration across a wide range of thermally sensitive polymers, advancing MPS and OoC platforms sensing capabilities.

Materials and methods

Fabrication of Teflon molds

Microfluidic devices were fabricated *via* soft lithography *via* custom-designed Teflon molds. The molds were designed *via* VCarve Pro 9.5 software (Vectric, UK) and machined from 4 mm thick Teflon sheets *via* a computer numerically controlled (CNC) milling system (Roland MDX-40A, Roland DG Corporation, USA). Three separate molds were fabricated, each corresponding to the three structural layers of the microfluidic devices: the upper layer (containing inlet and outlet ports), the middle layer (housing the microfluidic channel), and the bottom layer (serving as a sealing base with the integrated sensors). For the toxicity assay, molds with 4 × 12 mm cross sections and thicknesses of 1, 2, and 3 mm were used to fabricate the OSTE+ pieces.

Device fabrication with oxygen-scavenging properties

Devices were fabricated using Ostemer® 322 Crystal Clear (Ostemer 322, Mercene Labs AB, Sweden). The polymer resin was prepared by mixing components A and B at a 1.09 : 1 weight ratio, followed by degassing in a vacuum chamber for at least 2 h to eliminate bubbles. The degassed mixture was poured into Teflon molds, and excess resin was removed using a slab to achieve a smooth surface. The molds were

then subjected to a two-step curing process. The first cure involved UV (365 nm) exposure at 1000 mJ cm^{-2} for 20 s. After the initial UV curing, parts were demolded with flat tweezers and underwent a second thermal cure at either 30, 60, or 110 °C, depending on the experimental conditions. For control experiments, electrodes were integrated into a cyclic olefin copolymer (COP, Microfluidic ChipShop, Germany) substrate, and 1 mm thick poly(methyl methacrylate) (PMMA) served as the structural layer for non-oxygen-scavenging microfluidic devices. The PMMA layers were laser cut to match the dimensions of the OSTE+ microfluidic device. Both the oxygen-scavenging and control devices were assembled using double-sided pressure-sensitive adhesive (ARCare 8939; Adhesive Research Europe). The layers were then aligned and bonded under 2 kN pressure for 10 min using a PW-H laboratory press (P-O Weber, Germany) at room temperature to ensure uniform adhesion.

Inkjet printing

Printing was performed on UV-cured OSTE+ substrates to take advantage of their thiol-rich surface chemistry. Silver nanoparticle ink (DGP-40LT-15C; Advanced Nano Products, South Korea) was used for the pseudoreference electrode (pRE). Gold nanoparticle ink (Au-LT-20; Fraunhofer IKTS, Germany) was used for the working and counter electrodes (WE and CE). Both inks were deposited using the drop-on-demand Dimatix Materials Printer (DMP 2831; Fujifilm Dimatix; USA), which features 16-nozzles with a 10 pl drop-size print head from which 1, 2, or 3 adjacent nozzles were selected for deposition. Drop spacings for the inks and the substrates used are shown in Table 1.

The printer system maintained the substrate at 30 °C during ink deposition for OSTE+. Comparative printing was performed on 125 μm thick polyethylene terephthalate (PET) and 1 mm COP substrates. Prior to printing, these substrates were exposed to oxygen plasma for 60 s at a power of 80 W using plasma treatment machine (Smart Plasma 80 W-Oxygen, Plasma Technology, Germany) to improve ink adhesion. For PET and COP, the printer platen temperature was maintained at 60 °C to facilitate solvent evaporation.

Photonic and thermal sintering process

After ink deposition, sintering was carried out using a PulseForge Digital Thermal Processing™ system (NovaCentrix, USA). The samples were positioned 10 cm from the lamp and processed under ambient atmospheric conditions. The photonic curing parameters were optimized separately for the silver and gold nanoparticle inks to minimize the number of pulses required for complete sintering. The pulse duration was fixed at 600 μs, while the applied voltage was varied from 250 V to 500 V, corresponding to an incident energy range of 0.163 to 2.53 J cm^{-2}. For the PET substrates, thermal sintering was performed in a convection oven at 150 °C for 1 hour. After curing, the electrodes were passivated using a biocompatible, double-sided pressure-sensitive adhesive, ensuring that only the active electrode area remained exposed for subsequent measurements or functionalization. SimPulse software was used to simulate the thermal profile during the photonic curing process.

Table 1 Drop spacings used for inkjet printing of silver and gold nanoparticle inks on the different substrates used

Drop spacing	OSTE+	COP	PET
Silver nanoparticle ink	40	60	55
Gold nanoparticle ink	20	40	35

Pseudoreference electrode development

All the electrochemical measurements were conducted using a PalmSens4 potentiostat (PalmSens4 BV, Netherlands). The inkjet-printed silver electrodes were electrochemically chlorinated to stabilize their potential for use as pseudoreference electrodes (pREs). For chlorination, all three electrodes (WE, CE, and pRE) were fully immersed in 0.1 M hydrochloric acid (HCl, Sigma-Aldrich). Cyclic voltammetry (CV) was then applied, scanning from −0.2 V to +0.2 V *versus* an external 2 mm in diameter Ag/AgCl reference electrode (DRIREF-2, World Precision Instruments), at a scan rate of 20 mV s^{-1}, for a minimum of five cycles. To evaluate the electrochemical stability of the pRE, open circuit potential (OCP) measurements were performed. The pRE was immersed in 3 M potassium chloride (KCl, Sigma-Aldrich) solution, and the potential was recorded over a period of 1 hour. During OCP measurements, the pRE was connected as the WE, and an external Ag/AgCl reference electrode was used as the reference electrode to complete the electrochemical cell.

Electrochemical characterization

Following electrochemical chlorination of the reference electrode, a 10 mM equimolar solution of potassium ferrocyanide and ferricyanide in 10 mM KCl was used to evaluate the performance of the printed electrode system. CV was performed over a potential window of −0.2 V to +0.5 V at a scan rate of 25 mV s^{-1}. Three sequential configurations were assessed in the following order: first, the inkjet-printed WE was evaluated together with a commercial platinum wire CE and a commercial Ag/AgCl RE. Second, the platinum wire CE was replaced by an inkjet-printed CE. Finally, the fully printed three-electrode system was evaluated. The inkjet-printed CE was designed to be three times the size of the WE to avoid current limitations during measurements. In cases where the CV curve exhibited flattened redox peaks and a reduced current response (indicative of a limited electroactive surface area), an electrochemical activation step was applied. The activation consisted of five potential pulses alternating between −2.0 V and 0.0 V (*versus* Ag/AgCl), with 2 s pulse durations over a total stimulation time of 16 s in PBS, which was based on a protocol from A. Moya *et al.*[37] Following

activation, CV was repeated under identical conditions to assess improvement in the electrochemical response.

Electrode calibration

Oxygen electrodes were calibrated by preparing solutions with varying oxygen concentrations, which were achieved by adjusting the sulfite concentrations in the electrolyte solution. The oxygen concentration in each solution was measured using an optical dissolved oxygen meter (HANNA Instruments) prior to electrochemical measurements to correlate the electrode signal with the known oxygen content. To investigate the oxygen reduction reaction, linear sweep voltammetry (LSV) was performed over a potential window from 0.2 V to −0.9 V, with a scan rate of 25 mV s^{-1}. Following LSV, chronoamperometry was conducted at −0.8 V for each oxygen concentration. The potential was held for 60 s to allow the current to stabilize. The average current over the last 10 s of the chronoamperometric response was recorded and used to generate a calibration curve linking the steady-state current to the oxygen concentration, enabling quantitative analysis of the dissolved oxygen concentration.

Microfluidic characterization of the oxygen-scavenging properties

Microfluidic experiments were conducted to characterize the oxygen scavenging properties of OSTE+. All the experiments were performed at 25 °C in an incubator with 10 mM PBS solution. A custom-made PMMA holder was employed to securely seal the microfluidic tubing, preventing leakage and ensuring proper flow. Liquid perfusion was facilitated using a 4-channel peristaltic pump (Reglo ICC, ISMATEC, Cole-Parmer GmbH) with 2-stop pump tubing (Ismatec, PharMed® BPT) and silicone tubing (Freudenberg Medical). Microfluidic PEEK 1/16-inch fittings (XP-230X, IDEX Health & Science) were threaded into the holder, and stainless-steel tubing was used at the outlet to connect the microfluidic system to the oxygen sensor, preventing oxygen diffusion along the tubing. As a control, the oxygen concentrations at the outlet of the system were continuously measured *via* a commercial oxygen microsensor (UNISENSE, Denmark) integrated into a T-flow system and connected to a picometer controller (UNISENSE, Denmark). The microsensor was polarized at 0.8 V against an internal Ag/AgCl reference electrode. Before the experiments, the sensor was calibrated *via* a two-point procedure using an optical dissolved oxygen meter: one point in a solution at an atmospheric oxygen concentration and the second point in an oxygen-free solution.

Oxygen monitoring with inkjet-printed amperometric electrodes

Amperometric detection of dissolved oxygen was performed using a PalmSens4 potentiostat (PalmSens BV, Netherlands) in an incubator set at 25 °C. Devices were fabricated with inkjet-printed electrodes embedded in OSTE+ microfluidic platforms as described above. To evaluate the impact of thermal curing on oxygen scavenging and sensor performance, the chips were postcured for 1 hour at 30, 60, or 110 °C prior to electrochemical testing. Measurements were performed directly after fabrication. A control device was fabricated with inkjet-printed electrodes on a COP substrate and PMMA microfluidic parts, which lack oxygen scavenging capabilities, to evaluate the baseline oxygen profile. All devices were filled with 10 mM PBS, and chronoamperometry was performed by applying a constant potential of −0.8 V *versus* the printed Ag/AgCl reference electrode. Current measurements were recorded every 5 minutes over a total duration of 14 hours.

Oxygen consumption calculation

The oxygen consumption rate (mol O_2 per s) is directly proportional to the electrical current measured at the working electrode. To calculate oxygen consumption, the electrical current is first related to the number of electrons *via* the elementary charge constant (e = 1.6 × 10^{19} C). From the stoichiometry of the reaction, which involves 4 electrodes to reduce O_2 to H_2O^-, the number of oxygen molecules can be determined. Finally, when the Avogadro constant (NA = 6.022 × 1023 mol^{-1}) is used, the number of oxygen molecules is converted into moles of oxygen. This provides direct oxygen consumption for an electrochemical sensor.

Cytotoxicity assessment

To assess the acute cytotoxicity arising from potential leachable species released from Ostemer 322, two complementary experiments were performed. First, the polymer samples were cured at 30, 60, or 110 °C to evaluate whether biocompatibility is preserved at temperatures lower than the manufacturer's recommended 110 °C.[38] Second, to determine whether the amount of polymer influences biocompatibility and thereby the feasibility of fabricating devices of different dimensions under mild curing, additional samples of varying volumes (48, 96, and 144 mm^3) were tested at 30 °C since these conditions favor thiol retention and oxygen scavenging. The dimensions, surface areas, and volumes of the OSTE+ samples used in the cytotoxicity assessment are shown in Table 2.

For both experiments, cured polymer pieces were incubated in 1 mL of MEM Alpha medium with GlutaMAX

Table 2 Dimensions, surface areas, and volumes of the OSTE+ samples used in the cytotoxicity assessment. The A/V ratio is calculated as the sample surface area divided by the volume of the incubation medium (1 mL = 1000 mm^3)

Sample [mm]	Sample volume [mm^3]	Area [mm^2]	A/V ratio [mm^{-1}]
4 × 12 × 3	144	192	0.192
4 × 12 × 2	96	160	0.160
4 × 12 × 1	48	128	0.128

(Sigma-Aldrich) supplemented with 10% fetal bovine serum (FBS, Sigma-Aldrich) at 37 °C in a humidified incubator for 24 h, with each condition prepared in triplicate. Media incubated under identical conditions without polymer exposure served as negative control. Human intestinal colorectal adenocarcinoma cells (Caco-2, ECACC) were seeded in 24-well plates (Corning) and cultured for 5 days until they reached confluence. The cells were then exposed to the conditioned media and incubated for 24 h at 37 °C in a humidified incubator. Cell viability was assessed *via* the MTT assay (3-(4,5-dimethylthiazolyl-2)-2,5-diphenyltetrazolium bromide, Corning). MTT reagent was added to each well at a concentration of 5 mg mL^{-1} and incubated for 4 h, after which 100 μL of DMSO was added to dissolve the formazan crystals. The absorbance was measured at 570 nm using a UV-vis miniature spectrometer (Ocean Optics) with a halogen light source (HL-2000, Ocean Optics), and the cell viability was expressed relative to that of the untreated control.

Data analysis

Data representation was performed using GraphPad Prism 10 (GraphPad Software). Statistical significance was assessed using unpaired *t* tests; **** indicates $p < 0.0001$. The data are presented as the means ± standard deviations (SDs). All graphs that represent real-time data were generated with an on-purpose Python-based program to automate the data plotting process. For the chronoamperometry data, the values from the last 10 seconds were averaged and plotted.

Results

Photonic curing enables low-temperature sintering

OSTE+ has a glass transition temperature of 69 °C when fully cured according to the manufacturer's protocol at 110 °C. Above this temperature, the material softens and loses structural integrity, limiting high-temperature processing, such as conventional thermal sintering of printed

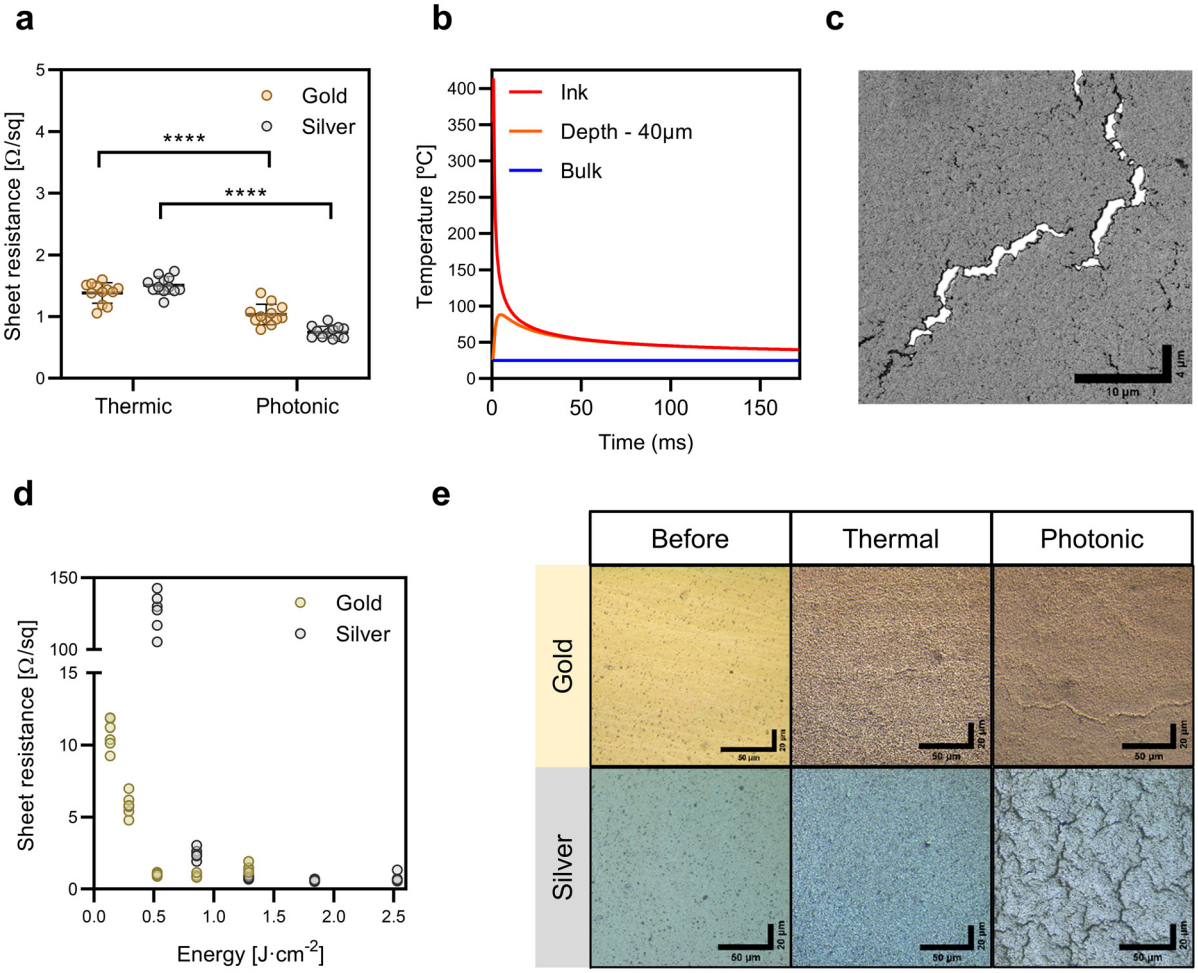

Fig. 1 Evaluation of photonic curing parameters for inkjet-printed gold and silver inks on PET substrates. a) Sheet resistance values of inkjet-printed gold and silver on PET substrate after thermal curing and photonic curing. b) Simulated thermal profile during photonic curing (600 μs, 400 V, 1.3 J cm^{-2}) showing spatial temperature gradients across the film thickness. Peak temperatures occur at the film surface (red), while temperature rapidly decreases toward the substrate interface (40 μm depth, orange), minimizing thermal load on the bulk material (blue). c) SEM image of a representative crack (~1.5 μm wide) observed in gold ink after photonic curing. d) Sheet resistance values of gold and silver inks as a function of photonic curing energy. e) Microscopy images of inkjet-printed gold and silver ink: (left) before sintering, (middle) after thermal curing, and (right) after photonic curing.

nanoparticle inks.[26] In contrast to conventional lithography-based or vacuum-deposited electrodes, the present approach enables direct electrode patterning on OSTE+ under low-temperature conditions compatible with its thiol functionality. The process avoids cleanroom fabrication, vacuum deposition, high-temperature treatment, and surface pretreatment steps to enhance metal–substrate adhesion, thereby facilitating the integration of sensing elements into temperature-sensitive polymers.

Because thermal sintering cannot be performed on OSTE+, PET was used as a model substrate to compare photonic curing against thermal sintering. PET tolerates the 150 °C required for thermal sintering, allowing direct comparison between the two methods. Compared to thermal sintering, photonic curing reduced the sheet resistance of gold and silver ink by 26% and 54%, respectively (Fig. 1a). This improvement is attributed to the high peak temperatures reached during photonic curing, up to 400 °C at the film surface without significantly heating the underlying substrate (Fig. 1b).[36] This rapid, localized heating enables processing in milliseconds without compromising substrate integrity. However, steep thermal gradients generated internal stress in the ink films, leading to crack formation (Fig. 1c). These effects are likely caused by rapid solvent evaporation and thermal stress triggered by high-intensity light pulses. To mitigate these effects, both the curing energy (Fig. 1d) and pulse number were optimized for both inks (SI Fig. S1). Effective sintering requires exceeding a minimum energy threshold to remove solvents, surfactants, and stabilizers, allowing nanoparticle coalescence. The optimal conductivity and minimal cracking occurred within an energy window of 0.8–1.3 J cm^{-2}, while higher energies sharply increased the crack density and ultimately disrupted electrical continuity (SI Fig. S2). The pulse number also influences performance, with two pulses yielding the lowest sheet resistance and variability. To compensate for surface defects and localized cracking, the number of printed layers was also optimized. Three layers of both the gold and silver inks ensured sufficient conductivity while maintaining mechanical integrity (SI Fig. S3). The morphological changes induced by curing were assessed by optical microscopy (Fig. 1e). Prior to sintering, the films displayed a uniform texture. Thermal curing led to moderate thickening, reflecting nanoparticle coalescence. Under optimized photonic curing conditions, more pronounced changes in microstructure were observed, including localized particle fusion and surface texturing, particularly in silver films.

Low-temperature oxygen sensor integration concept

OSTE+ retains unreacted thiol (-SH) groups after UV polymerization, which provides two key functionalities relevant for OoC/MPS systems. First, surface thiols allow direct covalent bonding with gold (Au) and silver (Ag) nanoparticles through gold–thiolate (Au–S) and silver–thiolate (Ag–S) interactions. This enables nanoparticle immobilization without additional surface modifications, providing an advantage over conventional substrates that typically require oxidative pretreatments such as oxygen plasma or chemical oxidants to improve adhesion.[39] Second, thiols confer oxygen-scavenging capabilities, which are enhanced by lowering the temperature of the second (thermal) curing step. This property allows precise tuning of the oxygen concentration within the device microenvironment, enabling the establishment of physiologically relevant conditions[35] (Fig. 2a).

As a proof of concept, a three-electrode amperometric oxygen sensor was designed, consisting of a gold working electrode (WE), a gold counter electrode (CE), and a pseudoreference electrode (pRE) based on Ag/AgCl. Oxygen reduction at the WE generates a current proportional to the oxygen concentration under an applied negative potential. This process can be observed by linear sweep voltammetry (LSV), which shows two distinct peaks at −0.4 and −0.8 V (LSV, SI Fig. S4). The first peak corresponds to the partial reduction of oxygen to hydrogen peroxide:

$$O_2 + 2H_2O + 2e^- \rightarrow H_2O_2 + 2OH^-$$

The second peak corresponds to the subsequent reduction of hydrogen peroxide to hydroxide ions:

$$H_2O_2 + 2e^- \rightarrow 2OH^-$$

This redox reaction occurs in a basic environment consistent with the pH of PBS (7.4). The electrodes were aligned in a single row, rather than in conventional circular designs, to minimize the footprint and facilitate integration into space-limited microfluidic devices (Fig. 2b). The WE and pRE each measured 500 μm in width, and the active sensing area was defined by a 2.6 mm opening, resulting in a WE area of 1.3 mm^2. The CE was designed to have three times the area of the WE to prevent current limitations.

The fabrication process is illustrated in Fig. 2c. First, substrate materials (step i), including OSTE+ and cyclic olefin polymer (COP), were selected. OSTE+ serves as the primary substrate because its unreacted thiol groups promote both strong metal adhesion and intrinsic oxygen-scavenging properties. COP was used as a nonreactive control to isolate the effects of the substrate on oxygen dynamics. Next, gold and silver nanoparticle inks were deposited *via* maskless inkjet printing: gold ink was printed first to define the WE and CE (step ii), followed by silver ink for the pRE and interconnects (step iii). The printed inks were then sintered by photonic curing with a xenon lamp (300–1100 nm), allowing rapid processing without thermal damage (step iv). A pressure-sensitive adhesive was patterned to passivate nonelectrochemical regions and define active sensing areas (step v). Finally, the silver pRE was electrochemically chlorinated to form a stable Ag/AgCl interface, ensuring a consistent reference potential. The measured OCP drift was 4.53 μV h^{-1} for Ag and 1.21 μV h^{-1} for Ag/AgCl (step vi, SI Fig. S5). This protocol enables the

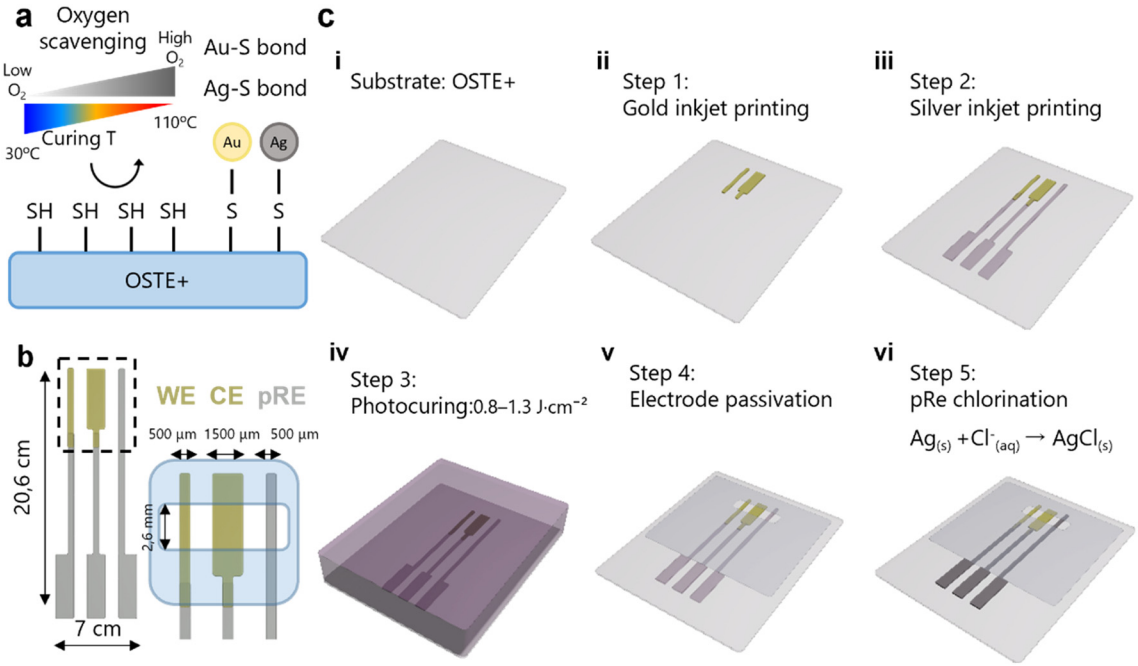

Fig. 2 Oxygen sensor integration *via* inkjet printing and photonic curing for temperature-sensitive substrates. a) Schematic representation of thiol group availability on OSTE+, enabling dual functionality: enhanced oxygen reduction with lower curing temperatures and strong gold–sulfur (Au–S) and silver–thiolate (Ag–S) bonding for robust sensor integration. b) Illustration of an amperometric oxygen sensor with gold WE and CE electrode and an Ag/AgCl pRE. c) Fabrication steps: (i) substrate selection, (ii) gold nanoparticle ink deposition, (iii) silver nanoparticle ink deposition, (iv) photonic curing for sintering, (v) passivation layer application to define active electrochemical areas, and (vi) pRE chlorination.

integration of functional electrochemical sensors on OSTE+ and other thermally sensitive materials.

Electrode integration into OSTE+

Inkjet-printed electrochemical sensor arrays with a three-electrode configuration were fabricated directly on OSTE+ substrates (Fig. 3a). Each unit included a WE, a CE, a pRE, and conductive tracks and pads (Fig. 3b). The OSTE+ surface after demolding from the Teflon mold *via* soft lithography mirrors the mold texture, resulting in an increased effective surface area for nanoparticle adhesion (Fig. 3c, top left). This roughness is preserved in the inkjet-printed gold and silver electrodes (top right and bottom left), further contributing to robust metal-polymer interfaces and a continuous Au–Ag junction (bottom right). The preserved surface texture prevents direct bonding between OSTE+ layers. Therefore, device assembly required an additional adhesive layer that also served as a structured passivation layer, introducing an additional fabrication step. The dimensional deviations of the fabricated electrodes compared with the designed electrodes were less than 5% (SI Fig. S6). This error is consistent with well-known sources of variability in the inkjet printing process, including the presence of dust particles on the substrate, missing or mis-ejected droplets, satellite droplets, and irregular droplet formation.[40] In addition, dimensional deviations may arise from droplet coalescence, solvent evaporation dynamics, and nanoparticle shrinkage during sintering. Surface roughness of OSTE+ further influences droplet spreading and edge definition, contributing to minor geometric variations. For these electrodes, the observed geometric variability did not measurably affect electrochemical performance. The electrodes on OSTE+ had a lower sheet resistance than those on PET, with average values reduced by 50% for both the OSTE+ and the gold and silver inks (Fig. 3d). This was achieved using a photonic curing energy of 1.29 J cm^{-2} with six printed layers for gold and four for silver (Fig. 3e and f). However, the optimal curing energy window was narrower for OSTE+ (Fig. 3e) than for PET (Fig. 2d). This behavior may be linked to differences in substrate thickness and thermal properties. The greater thickness of OSTE+ (1 mm) compared with PET (125 µm) may lead to localized heat retention during curing, enhancing ink sintering but increasing the risk of thermal degradation. Cyclic voltammetry (CV) revealed passivated electrodes characterized by a low current response, which increased after electrochemical activation, with well-defined redox peaks and a symmetric shape (Fig. 3g). The CV profiles were consistent across configurations: (i) printed WEs with commercial CEs and REs, (ii) printed WEs and CEs with commercial REs, and (iii) fully printed electrodes, resulting in consistent profiles (Fig. 3h). A slight potential shift of 30 mV was observed with the printed pRE, which can be attributed to differences in chloride concentration. Finally, the comparable CV responses of OSTE+ and PET confirmed the equivalent electrochemical behavior of this low-temperature curing protocol (Fig. 3i). The anodic–cathodic peak separation (ΔE_p) was 130 mV for OSTE+ and 100 mV for PET, reflecting quasireversible electron transfer. For comparison, ΔE_p is 59 mV for an ideal reversible

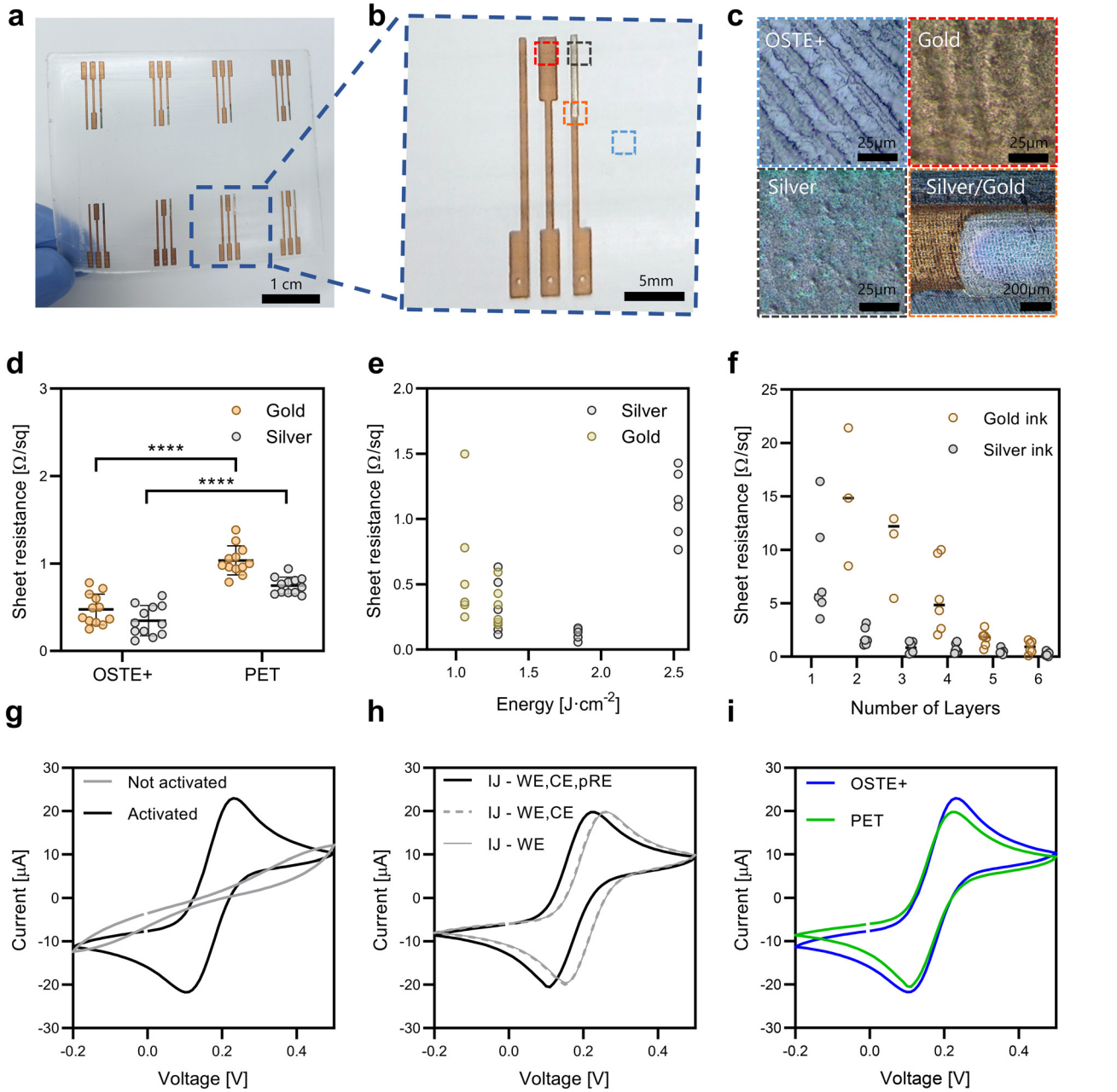

Fig. 3 Inkjet-printed gold and silver electrodes on OSTE+. a) Photograph of a sensor array inkjet printed on OSTE+ substrate. b) Close-up of a single electrochemical sensor showing its three-electrode configuration: working electrode (WE), counter electrode (CE), and pseudoreference electrode (pRE). c) Microscopy images showing: (top left) textured surface of cured OSTE+; (top right and bottom left) surface morphology of inkjet-printed gold and silver electrodes, respectively; and (bottom right) gold–silver interface. d) Comparison of electrode sheet resistance for gold and silver inks printed on PET and OSTE+ substrates after optimized photonic curing. e) Electrode sheet resistance as a function of photonic curing energy for gold and silver inks on OSTE+. f) Resistivity values of gold and silver inks as a function of the number of inkjet-printed layers on OSTE+ substrate. g–i) Electrochemical performance in 10 mM ferro/ferricyanide solution at a scan rate of 20 mV s^{-1} g) cyclic voltammograms (CVs) before and after electrochemical activation of the WE in OSTE+. h) CVs comparing electrode configurations using inkjet-printed WE and commercial CE and pRE (line IJ-WE), using inkjet-printed WE and CE and commercial pRE (line IJ-WE, CE and all integrated inkjet-printed electrodes (line-WE, CE, and pRE) i) CVs comparing sensor performance on different substrates: OSTE+ and PET.

one-electron transfer at 25 °C. The slightly larger ΔE_p and increased CV area on OSTE+ may be associated with the rougher substrate texture, which increases the effective electroactive surface area and introduces minor heterogeneities in electron-transfer kinetics.

Electrochemical electrode characterization and calibration

Following electrode integration into OSTE+ for dissolved oxygen measurements, the same fabrication protocol was applied to COP, a polymer lacking intrinsic oxygen-scavenging properties (SI Fig. S7). COP served as a control to

isolate the contribution of OSTE+ thiol chemistry to oxygen reduction. Moreover, since electrochemical sensing consumes dissolved oxygen, COP confirmed that the oxygen depletion observed for OSTE+ originates from its thiol-based surface chemistry rather than electrochemical consumption. CVs from electrodes on both substrates exhibited similar redox peak shapes and currents, indicating reproducible and electrochemically equivalent sensor performance (n = 12, Fig. 4a. To qualitatively confirm oxygen reduction at the WE, LSV was conducted on both substrates (Fig. 4b), revealing a current increase with a negative potential consistent with dissolved oxygen reduction. The calibration curves revealed a linear relationship between the current response and dissolved oxygen concentration (0–8 mg L^{-1}, equivalent to 0–21% atmospheric O_2), with a sensitivity of 0.15 μA L mg^{-1} for both substrates. (Fig. 4c). A slight offset toward more negative potentials was observed for COP, suggesting less favorable oxygen reduction kinetics than those of OSTE+. The sensor response time was evaluated through four consecutive chronoamperometric measurements at a constant oxygen concentration. The devices on OSTE+ had an average response time of 9.3 ± 3.9 s, whereas those on COP had an average response time of 8.2 ± 1.6 s (Fig. 4d). These data demonstrate that both substrates support reliable low-temperature sensor integration with equivalent sensitivity and response times. The favorable thiol chemistry in OSTE+ likely facilitates strong metal–thiol interactions, which may contribute to enhanced oxygen reduction kinetics. Beyond electrochemical performance, we evaluated the electrode adhesion on OSTE+ and COP using the standard scotch tape test (SI Fig. S8). On untreated COP substrate, electrodes delaminated readily. Plasma treatment of COP prior to printing improved adhesion. However, electrodes printed on OSTE+ did not require any plasma treatment for adhesion, as no visible delamination after tape testing was observed. This confirms that the thiol-rich surface of OSTE+ enables robust metal–polymer adhesion, eliminating the need for surface activation steps required for inert polymers like COP.

Comparison of the oxygen-scavenging efficiency of OSTE+ and COP

To demonstrate that the low-temperature fabrication strategy enables effective sensor integration, a multilayered OSTE+

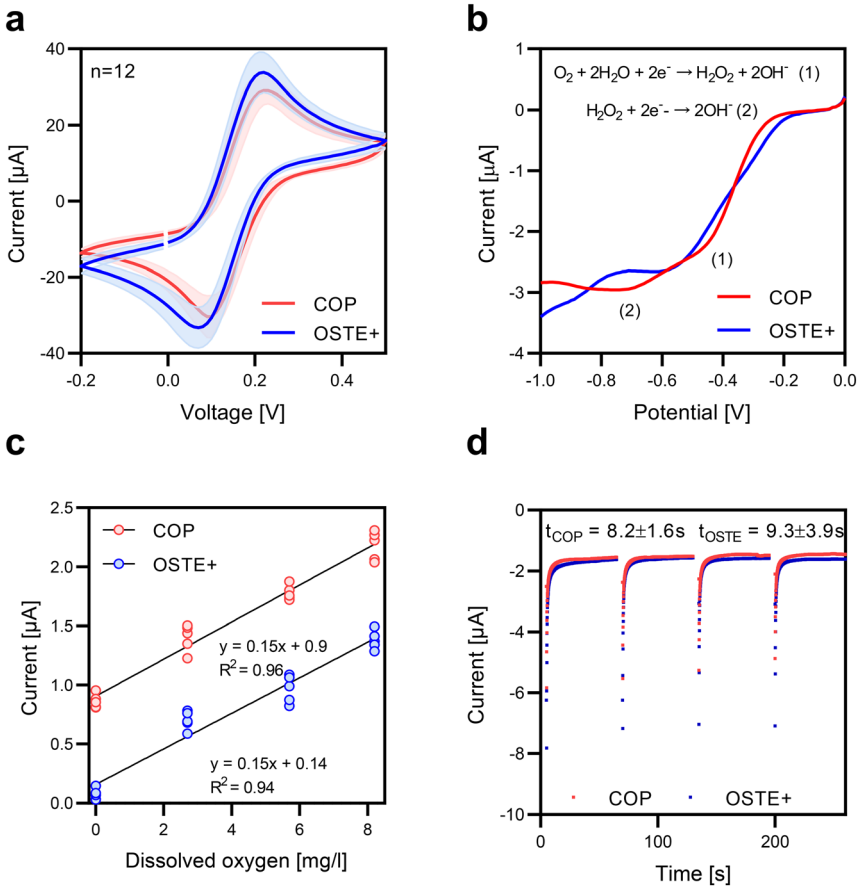

Fig. 4 Electrochemical characterization and calibration for oxygen sensing. a) CVs of electrodes inkjet printed on OSTE+ and COP substrates (n = 12). b) LSV on OSTE+ and COP in 10 mM PBS, showing the reduction of oxygen when a negative voltage window is applied from 0 to −1 V. c) Calibration curves showing current density (μA cm^{-2}) response as a function of dissolved oxygen concentration (mg l^{-1}) for the same electrodes integrated into OSTE+ and COP substrates (n = 4). d) Four consecutive chronoamperometric measurements in 10 mM PBS, each lasting 60 seconds, assessing the response time at a fixed dissolved oxygen concentration on OSTE+ and COP substrates (n = 4).

microfluidic device with integrated inkjet-printed oxygen sensors was fabricated. The device consisted of three cast OSTE+ layers, with a channel (width: 2.6 mm, length: 22.6 mm, height: 1 mm) incorporated in the middle layer, resulting in a surface-to-volume ratio of 2.77 mm^{-1} (162.72 mm^2/58.76 mm^3) (Fig. 5a). The sensor was positioned at the center of the channel to enable real-time monitoring of dissolved oxygen. For fabrication and testing, four identical units were prepared in parallel on a single platform (Fig. 5b). The devices cured at 30 °C demonstrated the highest oxygen-scavenging efficiency, which was consistent with the maximal retention of unreacted thiol groups. Increasing the curing temperature to 60 °C and 110 °C resulted in a progressively reduced scavenging capacity (Fig. 5c). Oxygen scavenging rationale has been previously studied by Kiiski and colleagues, who also investigated the effects of thermal post-processing.[41] While commercial OSTE+ formulation include an additional heat-curable epoxy component, both OSTE and

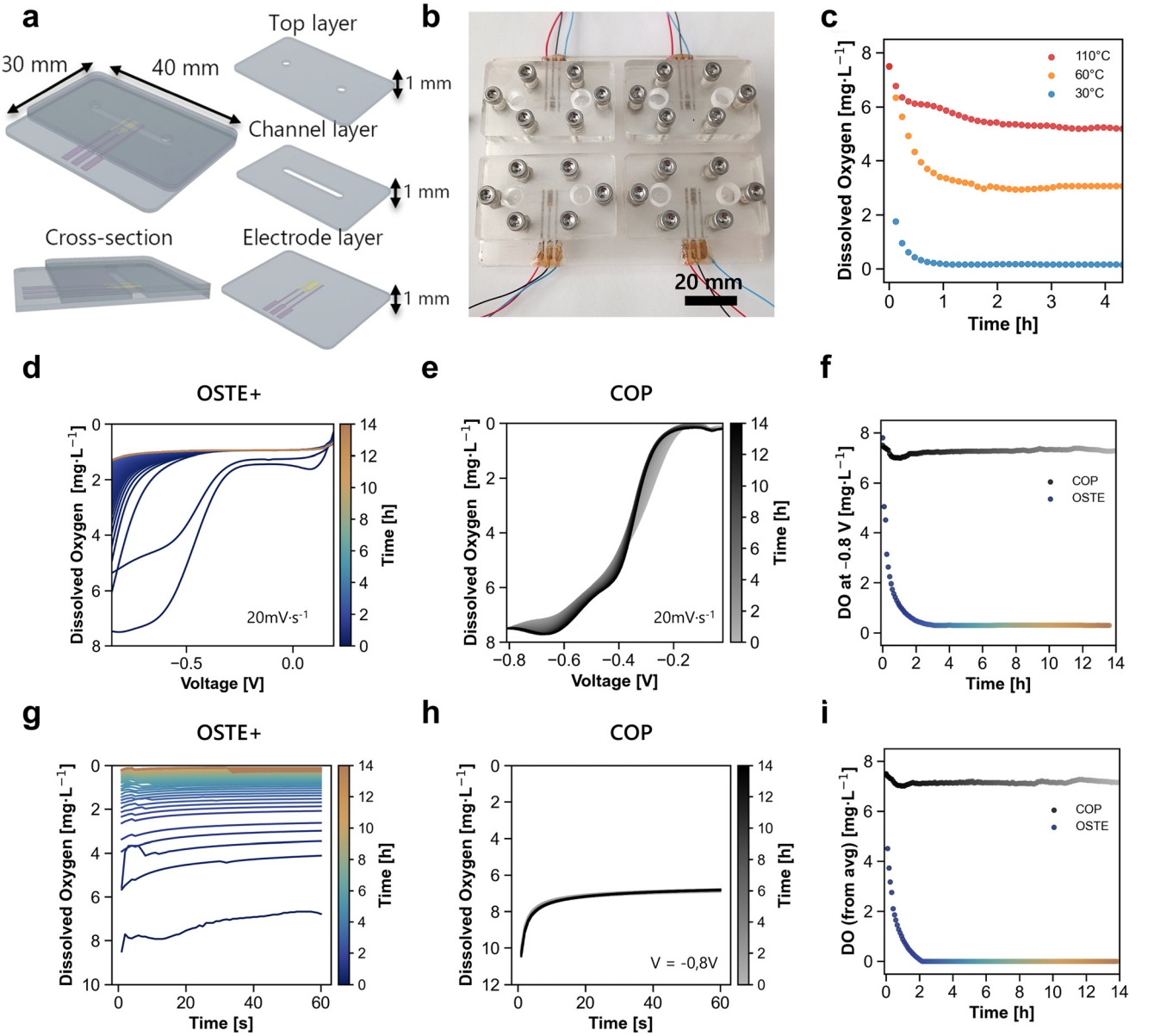

Fig. 5 Oxygen reduction dynamics in OSTE+ *versus* COP microfluidic devices. a) Schematic of the device structure, comprising three layers: bottom (electrode layer), middle (microfluidic channel), and top sealing layer. A cross-sectional view depicts the internal channel structure. b) Photograph of four identical devices, each with a single integrated oxygen sensor, on one platform. c) Dissolved oxygen concentration over time measured in microfluidic devices cured at 30, 60, and 110 °C during the second thermal curing step. (d and e) LSV in PBS from 0 to −0.8 V at 20 mV s^{-1}, every 5 min over 14 h. OSTE+ devices (d) show progressive oxygen depletion, while COP devices (e) remain electrochemically stable, indicating no scavenging activity. f) Current at −0.8 V extracted from LSV, highlighting the difference in oxygen consumption between OSTE+ and COP. g and h) Chronoamperometry in PBS at −0.8 V over 60 s, every 5 min for 14 h. OSTE+ devices (g) show increasing oxygen reduction, while COP devices (h) remain stable. Devices fabricated with (g) OSTE+ again exhibit oxygen reduction, while (e) COP shows stable response. i) Comparison of OSTE+ and COP dynamics based on the average current during the final 10 s of each chronoamperometric measurement.

OSTE+ share a thiol–ene backbone and exhibit qualitatively similar temperature-dependent oxygen scavenging behavior. These observations suggest that thiol-mediated reactions play a central role in oxygen depletion across different OSTE-based formulations, while curing temperature modulates the availability of reactive groups.

LSV scans from 0 to −0.8 V in PBS were performed every 5 min over 14 hours under static conditions. OSTE+ devices cured at 30 °C showed a progressive decrease in dissolved oxygen, indicating spontaneous oxygen scavenging upon contact with aqueous media (Fig. 5d). In contrast, COP controls exhibited stable LSV profiles with two well-defined reduction peaks (Fig. 5e). Current quantification at −0.8 V, corresponding to complete oxygen reduction, revealed rapid oxygen depletion within 2 hours for OSTE+, whereas the COP showed no significant change (Fig. 5f). Chronoamperometry at −0.8 V for 60 s every 5 min confirmed these trends (Fig. 5g and h), with the average dissolved oxygen during the last 10 s further validating the oxygen depletion in OSTE+ and the stability of the COP (Fig. 5i).

Cytotoxicity assays using Caco-2 cells exposed to polymer supernatants from samples cured at 30, 60, and 110 °C revealed no significant reduction in viability compared with untreated controls, confirming that OSTE+ remains biocompatible even at curing temperatures lower than the manufacturer's recommended 110 °C (SI Fig. S9a and b). To further examine whether the amount of polymer influences cytotoxicity, additional assays performed at 30 °C with varying volumes (48, 96, and 144 mm^3) also revealed no detectable effect on cell viability (SI Fig. S9c). These experiments provide a preliminary assessment of acute cytotoxicity arising from potential leachable species released from OSTE+ under different curing temperature and volume conditions. Together, these results demonstrate that the oxygen scavenging capacity is modulated by the curing temperature, reflecting differences in thiol retention. This tunable behavior is particularly important for generating physiologically relevant oxygen profile levels in MPS and OoC platforms.

Real-time monitoring of oxygen gradients in an OSTE+ microfluidic device for OoC models

To resolve spatial oxygen dynamics under perfusion, a multilayer microfluidic device with three integrated inkjet-printed sensors was fabricated (Fig. 6a). All the layers were cast from OSTE+ and measured 1 mm thick. The middle layer contains a serpentine channel (width: 2.6 mm, length: 205 mm), resulting in a surface to volume ratio of 2.77 mm^{-1} (Fig. 6b). The bottom layer incorporates three sensors at the inlet, middle, and outlet positions, whereas the top layer serves as a cover (Fig. 6c). Initial characterization of oxygen scavenging employed a commercial electrochemical sensor inserted into a T-junction, where measurements were taken upstream of the device under flow conditions. Evaluation of the curing temperature, flow rate, channel surface area, and post-fabrication time revealed distinct dissolved oxygen modulation profiles (SI Fig. S10). Subsequent experiments with integrated sensors were performed on devices cured at 30 °C with a 550 mm^2 surface area immediately after fabrication to enhance oxygen scavenging. Devices were operated at a flow rate of 10 μl min^{-1}, optimizing the residence time for oxygen scavenging. Chronoamperometric measurements at the inlet, middle, and outlet electrodes over 18 hours (Fig. 6d–f) revealed rapid oxygen depletion, establishing a stable gradient within the first hour (Fig. 6h). The dissolved oxygen concentration decreased from 7.5 mg L^{-1} to ~1.0, 0.5, and <0.08 mg L^{-1} at the inlet, middle, and outlet, respectively. These dissolved oxygen levels at the outlet are in agreement with measurements obtained using the commercial sensor. COP-based controls maintained stable oxygen levels (~7.5 mg L^{-1}) throughout, confirming that scavenging is specific to OSTE+.

These results demonstrate the ability to precisely control and monitor physiologically relevant oxygen gradients with OSTE+ polymers, highlighting its potential for advanced OoC/MSP applications requiring oxygen control. Unlike existing oxygen sensors, which are typically limited to monitoring, the presented approach leverages the thiol–ene chemistry of OSTE+ to both measure and scavenge oxygen within the same integrated platform (see SI Table S1 for a detailed comparison with commercial and research sensors). This dual functionality positions the device as a versatile tool for advanced OoC/MPS models requiring microenvironment oxygen control and sensing.

Conclusion

This study demonstrates a low-temperature photonic curing protocol for the direct integration of inkjet-printed electrochemical sensors within OSTE+ microfluidic devices. OSTE+ is a thiol-rich polymer that provides unique advantages for sensor integration. Its residual thiol groups enable direct immobilization of conductive nanoparticles such as gold and silver *via* strong thiol–metal interactions, facilitating stable electrode fabrication. The optimized curing energy of approximately 1.29 J cm^{-2} achieved minimal electrode resistivity and cracking, producing high-fidelity electrode patterns with reproducible electrochemical performance. Notably, the electrodes on OSTE+ exhibited approximately 50% greater conductivity than did those on conventional PET substrates without requiring any substrate pretreatment. Moreover, the protocol was successfully applied across multiple substrates, including PET and COP, which are relevant for OoC and MPS.

Beyond the specific oxygen-sensing application, this work establishes a low-temperature fabrication strategy for the integration of metallic sensing elements on thermally sensitive polymer substrates. By combining inkjet printing with photonic curing, conductive patterns can be established without bulk thermal exposure. Although demonstrated here

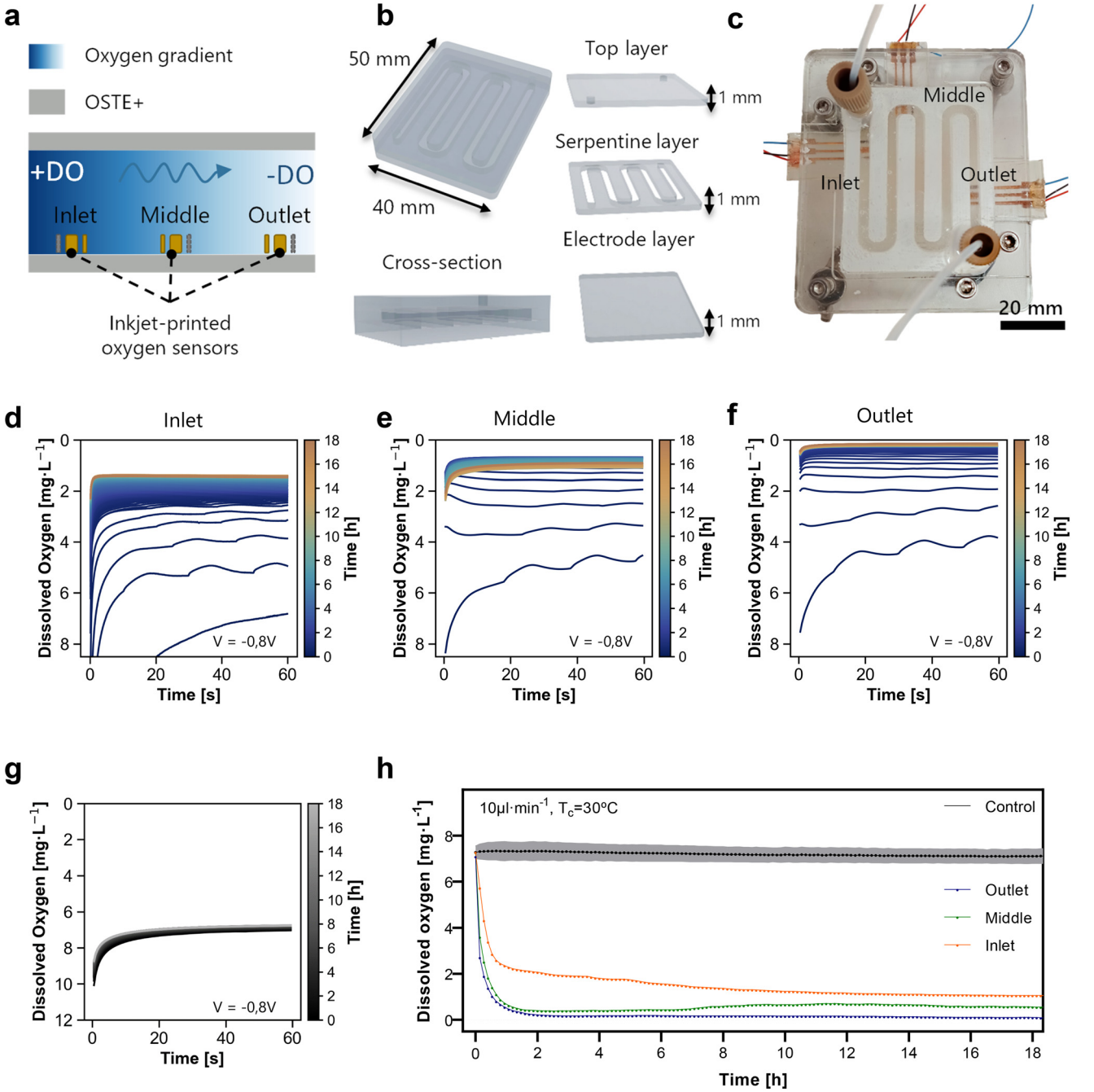

Fig. 6 Integration of electrochemical oxygen sensors into an OSTE+ microfluidic device for spatial and temporal monitoring under flow. a) Schematic depicting spatial oxygen gradients along the channel, with electrochemical sensors positioned at the inlet, middle, and outlet for spatially resolved sensing. b) Photograph of the assembled microfluidic device fabricated from OTE+. c) Schematic of the device structure, comprising three layers: bottom (electrode layer), middle (microfluidic channel), and top sealing layer. A cross-sectional view depicts the internal channel structure. d–f) Chronoamperometric oxygen measurements acquired over 60 seconds every 5 min over 18 h at the inlet (d), middle (e), and outlet (f) electrodes of the OSTE+ device. Current signals were converted to oxygen concentrations using calibration curves. g) Chronoamperometric response from a COP-based control device under equivalent conditions. h) Long-term oxygen measurements over 18 hours at the inlet, middle, and outlet electrodes under continuous flow (10 µL min^{-1}) and a thermal curing temperature of 30 °C. A COP-based device was included as a nonscavenging control (n = 3).

with an electrochemical oxygen sensor on OSTE+, this low-temperature integration approach is compatible with a broader range of sensing modalities and temperature-sensitive polymers.

By combining the intrinsic oxygen-tunable capacity of OSTE+ with low-temperature sensor integration, this work presents a strategy for both recreating and monitoring precise oxygen levels on-chip. This capability is particularly

critical for modeling organs with specific oxygen tensions (*e.g.*, the gut, liver, and brain), pathophysiological microenvironments (*e.g.*, tumors and ischemic regions such as stroke), or the creation of controlled hypoxic and near-anoxic conditions *in vitro*. The fabricated OSTE+ microfluidic devices enable real-time and on-chip monitoring of dissolved oxygen levels while simultaneously modulating oxygen concentrations, representing a significant advance toward material-driven, multifunctional platforms for advanced OoC and MPS.

Conflicts of interest

The authors declare that there is no conflict of interest.

Data availability

Data for this article, including different types of data from optical images, SEM, simulation data, electrochemical characterization, and dissolved oxygen values are available at Zenodo at https://doi.org/10.5281/zenodo.17672121.

Acknowledgements

IMB-CNM is supported by the María de Maeztu Units of Excellence programme (Grant CEX2023-001397-M), funded by MCIU/AEI/10.13039/501100011033. The authors acknowledge support from the Ministerio de Ciencia Innovación y Universidades (MICIU/FEDER, EU) in Spain through the GUMICHIP project (RTI2018-096786-B-I00). Denise Marrero acknowledges that this work has been done within the framework of the Ph.D. program in Electrical and Telecommunication Engineering at the Universitat Autònoma de Barcelona and was supported by the FPI Ph.D fellowship (PRE2019-089214). This work has made use of the Spanish ICTS Network MICRONANOFABS partially supported by MICINN and the ICTS 'NANBIOSIS', more specifically by the Micro-NanoTechnology Unit of the CIBER in Bioengineering, Biomaterials and Nanomedicine (CIBER-BBN) at the IMB-CNM. This research was supported by CIBER -Consorcio Centro de Investigación Biomédica en Red- (CB06/01/0049), Instituto de Salud Carlos III, and Ministerio de Ciencia e Innovación. Cytotoxicity experiments were performed at Servei de Cultius Cel·lulars, Producció d'Anticossos i Citometria (SCAC), which belongs to the Universitat Autònoma de Barcelona (UAB). This work was also supported by the Generalitat de Catalunya (2021SGR00495).

References

1 E. Ferrari, C. Palma, S. Vesentini, P. Occhetta and M. Rasponi, *Biosensors*, 2020, **10**, 110.
2 D. Marrero, F. Pujol-Vila, D. Vera, G. Gabriel, X. Illa, A. Elizalde-Torrent, M. Alvarez and R. Villa, *Biosens. Bioelectron.*, 2021, **181**, 113156.
3 Y. Zhu, K. Mandal, A. L. Hernandez, S. Kawakita, W. Huang, P. Bandaru, S. Ahadian, H.-J. Kim, V. Jucaud, M. R. Dokmeci and A. Khademhosseini, *Curr. Opin. Biomed. Eng.*, 2021, **19**, 100309.
4 S. G. Higgins, A. Lo Fiego, I. Patrick, A. Creamer and M. M. Stevens, *Adv. Mater. Technol.*, 2020, **5**, 2000384.
5 D. Marrero, A. Guimera, L. Maes, R. Villa, M. Alvarez and X. Illa, *Lab Chip*, 2023, **23**, 1825–1834.
6 N. Renous, M. D. Kiri, R. A. Barnea, R. Rauti, Y. Leichtmann-Bardoogo and B. M. Maoz, *Lab Chip*, 2022, **22**, 71–79.
7 J. Yeste, L. Martínez-Gimeno, X. Illa, P. Laborda, A. Guimerà, J. P. Sánchez-Marín, R. Villa and I. Giménez, *Biotechnol. Bioeng.*, 2018, **115**, 1604–1613.
8 J. Dornhof, J. Kieninger, H. Muralidharan, J. Maurer, G. A. Urban and A. Weltin, *Lab Chip*, 2022, **22**, 225–239.
9 M. A. U. Khalid, K. H. Kim, A. R. Chethikkattuveli Salih, K. Hyun, S. H. Park, B. Kang, A. M. Soomro, M. Ali, Y. Jun, D. Huh, H. Cho and K. H. Choi, *Lab Chip*, 2022, **22**, 1764–1778.
10 A. Moya, M. Ortega-Ribera, X. Guimerà, E. Sowade, M. Zea, X. Illa, E. Ramon, R. Villa, J. Gracia-Sancho and G. Gabriel, *Lab Chip*, 2018, **18**, 2023–2035.
11 S. Jalili-Firoozinezhad, F. S. Gazzaniga, E. L. Calamari, D. M. Camacho, C. W. Fadel, A. Bein, B. Swenor, B. Nestor, M. J. Cronce, A. Tovaglieri, O. Levy, K. E. Gregory, D. T. Breault, J. M. S. Cabral, D. L. Kasper, R. Novak and D. E. Ingber, *Nat. Biomed. Eng.*, 2019, **3**, 520–531.
12 F. Pujol-Vila, P. Giménez-Gómez, N. Santamaria, B. Antúnez, N. Vigués, M. Díaz-González, C. Jiménez-Jorquera, J. Mas, J. Sacristán and X. Muñoz-Berbel, *Sens. Actuators, B*, 2016, **222**, 55–62.
13 D. Sanahuja, P. Giménez-Gómez, N. Vigués, T. N. Ackermann, A. E. Guerrero-Navarro, F. Pujol-Vila, J. Sacristán, N. Santamaria, M. Sánchez-Contreras, M. Díaz-González, J. Mas and X. Muñoz-Berbel, *Lab Chip*, 2015, **15**, 1717–1726.
14 Q. Wu, P. Zhang, G. O'Leary, Y. Zhao, Y. Xu, N. Rafatian, S. Okhovatian, S. Landau, T. A. Valiante, J. Travas-Sejdic and M. Radisic, *Biofabrication*, 2023, **15**, 035023.
15 J. U. Lind, T. A. Busbee, A. D. Valentine, F. S. Pasqualini, H. Yuan, M. Yadid, S.-J. Park, A. Kotikian, A. P. Nesmith, P. H. Campbell, J. J. Vlassak, J. A. Lewis and K. K. Parker, *Nat. Mater.*, 2017, **16**, 303–308.
16 A. Bussooa, E. Tubbs, F. Revol-Cavalier, A. Chmayssem, M. Alessio, M.-L. Cosnier and N. Verplanck, *Biosens. Bioelectron.: X*, 2022, **11**, 100198.
17 N. Rahav, D. Marrero, A. Soffer, E. Glickman, M. Beldjilali-Labro, Y. Yaffe, K. Tadmor, Y. Leichtmann-Bardoogo, U. Ashery and B. M. Maoz, *Adv. Sci.*, 2024, **11**, 2305555.
18 M. W. Van Der Helm, M. Odijk, J.-P. Frimat, A. D. Van Der Meer, J. C. T. Eijkel, A. Van Den Berg and L. I. Segerink, *Biosens. Bioelectron.*, 2016, **85**, 924–929.
19 M. W. Toepke and D. J. Beebe, *Lab Chip*, 2006, **6**, 1484.
20 L. B. Neves, I. S. Afonso, G. Nobrega, L. G. Barbosa, R. A. Lima and J. E. Ribeiro, *Micromachines*, 2024, **15**, 670.
21 J. Wu, R. Wang, H. Yu, G. Li, K. Xu, N. C. Tien, R. C. Roberts and D. Li, *Lab Chip*, 2015, **15**, 690–695.
22 K. J. Lee, K. A. Fosser and R. G. Nuzzo, *Adv. Funct. Mater.*, 2005, **15**, 557–566.

23 T. Tsuzuki, K. Baassiri, Z. Mahmoudi, A. S. Perumal, K. Rajendran, G. M. Rubies and D. V. Nicolau, *Materials*, 2022, **15**, 2313.
24 D. Sticker, R. Geczy, U. O. Häfeli and J. P. Kutter, *ACS Appl. Mater. Interfaces*, 2020, **12**, 10080–10095.
25 T. Haraldsson, C. F. Carlborg and W. Van Der Wijngaart, OSTE: a novel polymer system developed for Lab-on-Chip, *Proc. SPIE 8976, Microfluidics, BioMEMS, and Medical Microsystems XII*, 2014, p. 897608.
26 N. Sandström, R. Z. Shafagh, A. Vastesson, C. F. Carlborg, W. Van Der Wijngaart and T. Haraldsson, *J. Micromech. Microeng.*, 2015, **25**, 075002.
27 J. P. Lafleur, R. Kwapiszewski, T. G. Jensen and J. P. Kutter, *Analyst*, 2013, **138**, 845–849.
28 P. Harris, J. Kaveh, A. M. Kemas, H. Mikaelsson, M. Fielden, V. M. Lauschke and Reza Zandi, *ACS Appl. Mater. Interfaces*, 2024, **11**, 2300972.
29 R. Rimsa, A. Galvanovskis, J. Plume, F. Rumnieks, K. Grindulis, G. Paidere, S. Erentraute, G. Mozolevskis and A. Abols, *Micromachines*, 2021, **12**, 546.
30 S. Das, A. Singh, V. R. Rao and T. Kundu, *ACS Appl. Polym. Mater.*, 2023, **5**, 9456–9465.
31 Y. Xue, X. Li, H. Li and W. Zhang, *Nat. Commun.*, 2014, **5**, 4348.
32 L. Zhen, M. Tian, G. Yang, Y. Chen, G. Li, Q. Zhang, Y. Li, P. Wan and J. Wu, *Signal Transduction Targeted Ther.*, 2022, **7**, 218.
33 V. Palacio-Castañeda, N. Velthuijs, S. Le Gac and W. P. R. Verdurmen, *Lab Chip*, 2022, **22**, 1068–1092.
34 Z. Yuan, *Microfluid. Nanofluid.*, 2022, **26**, 42.
35 D. Sticker, M. Rothbauer, J. Ehgartner, C. Steininger, O. Liske, R. Liska, W. Neuhaus, T. Mayr, T. Haraldsson, J. P. Kutter and P. Ertl, *ACS Appl. Mater. Interfaces*, 2019, **11**, 9730–9739.
36 K. A. Schroder, Mechanisms of photonic curing™: Processing high temperature films on low temperature substrates, *Technical Proceedings of the 2011 NSTI Nanotechnology Conference and Expo, NSTI-Nanotech 2011*, 2011, vol. 2, pp. 220–223.
37 A. Moya, E. Sowade, F. J. Del Campo, K. Y. Mitra, E. Ramon, R. Villa, R. R. Baumann and G. Gabriel, *Org. Electron.*, 2016, **39**, 168–176.
38 P. Aubrecht, J. Smejkal, P. Panuška, K. Španbauerová, V. Neubertová, P. Kaule, J. Matoušek, S. Vinopal, M. Liegertová, M. Štofik and J. Malý, *RSC Adv.*, 2024, **14**, 3617–3635.
39 J. C. Love, L. A. Estroff, J. K. Kriebel, R. G. Nuzzo and G. M. Whitesides, *Chem. Rev.*, 2005, **105**, 1103–1170.
40 E. Sowade, E. Ramon, K. Y. Mitra, C. Martínez-Domingo, M. Pedró, J. Pallarès, F. Loffredo, F. Villani, H. L. Gomes, L. Terés and R. R. Baumann, *Sci. Rep.*, 2016, **6**, 33490.
41 I. Kiiski, P. Järvinen, E. Ollikainen, V. Jokinen and T. Sikanen, *Lab Chip*, 2021, **21**, 1820–1831.

